

# Projected gravitational wave constraints on primordial black hole abundance for extended mass distributions

G. L. A. Dizon<sup>1</sup> and R. C. Reyes

National Institute of Physics,  
University of the Philippines - Diliman,  
Quezon City, Philippines

E-mail: [gldizon@nip.upd.edu.ph](mailto:gldizon@nip.upd.edu.ph)

**Abstract.** We investigate the projected minimum constraints set by next-generation gravitational wave detectors Einstein Telescope and LISA on the abundance of primordial black holes relative to dark matter from both resolvable mergers and the stochastic gravitational wave background (SGWB) for extended primordial black hole mass distributions. We consider broad power law distributions for a range of negative and positive exponents  $\gamma$  and top-hat distributions (with  $\gamma = 0$ ) and use the IMRPhenomXAS waveforms to simulate binary sources up to mass ratios  $q_{\max} = 1000$  and redshifts  $z = 300$ . Our results suggest that accounting for extended mass distributions have the most apparent impact when considering mergers at high redshifts  $z > 30$ , for which the constraint curves have broader mass windows and shift to higher abundances compared to when a monochromatic distribution is assumed; on the other hand, constraints from low-redshift mergers and the SGWB do not change much with the assumed mass distribution. At high redshifts, astrophysical black holes are not expected to contribute significantly, providing possible smoking-gun evidence for PBHs. Constraints derived from LISA and ET observations would complement each other by probing different PBH mass windows and this holds for the extended mass distributions studied.

**ArXiv ePrint:** [2406.12281](https://arxiv.org/abs/2406.12281)

---

<sup>1</sup>Corresponding author.

---

## Contents

<b>1</b>	<b>Introduction</b>	<b>1</b>
<b>2</b>	<b>Source and detector models</b>	<b>2</b>
2.1	Parameter initialization and GW waveforms	2
2.2	Calculating detector SNR	3
2.3	Mass distributions	5
2.3.1	Monochromatic mass distribution	5
2.3.2	Bounded power law mass distribution	5
<b>3</b>	<b>Calculating the constraining observables</b>	<b>6</b>
3.1	Expected detectable merger event rate	6
3.2	Expected stochastic GW background	8
<b>4</b>	<b>Constraints on PBH abundance</b>	<b>9</b>
4.1	Methodology	9
4.2	Constraints from resolvable mergers	10
4.3	Constraints from SGWB	15
4.4	Effect of varying maximum mass ratios	16
<b>5</b>	<b>Conclusions and outlook</b>	<b>16</b>

---

## 1 Introduction

Primordial black holes (PBHs) have long been considered a possible solution to the dark matter problem, with interest resurging due to their possible contribution to merger signals in gravitational wave (GW) detectors such as LIGO [1], along with more recent stochastic GW background (SGWB) measurements from pulsar timing arrays like NANOGrav probing potential PBH formation mechanisms [2, 3]. Constraints on PBH population abundance (relative to dark matter)  $f_{\text{PBH}}$  have been derived from various observations [4, 5] such as microlensing [6–14], CMB temperature data [15], as well as from dynamical [14, 16, 17] and structural [18] considerations for observed cosmological structures. While these constraints are well-established for both monochromatic [5] and extended mass distributions [14, 19–21], there is still a sizeable lack of constraints derived from GW data in the literature. Current GW-based constraints from existing [22–25] and projected observations [26, 27] either largely assume a monochromatic (or narrow-width) initial mass distribution of PBHs upon formation, or even with consideration of broad distributions only account for symmetric-mass binary mergers [28].

This paper extends part of existing work by De Luca, et al. [26] in projecting minimum PBH abundance constraints using simulated LISA and ET detector models. While they only report results for monochromatic mass distributions, here we consider extended mass functions with a simple power law form  $\psi(M) \propto M^{-\gamma}$  for both positive and negative values of  $\gamma$ , as well as for  $\gamma = 0$ , corresponding to a top-hat distribution; we allow for values of  $\gamma$  to admit both very narrow and very broad mass function widths. In order to fully capture the effect of such a range of mass functions, we consider binary mergers with mass

ratios up to  $q_{\max} = 1000$ , the maximum allowed by the range of validity of our assumed waveform approximant. We derive constraints from both resolvable mergers and the SGWB. For the former, we split our analysis between low-redshift ( $z \leq 30$ ) and high-redshift ( $z > 30$ ) mergers to investigate the impact of extended mass functions on the detectability of mergers at different redshift regimes.

We structure this paper as follows. Section 2 discusses the setup and assumptions on both PBH sources and detector models used to forecast constraints as well as the mass distributions considered. Section 3 outlines how the constraining observables are calculated, namely the expected detectable merger event rate for resolvable mergers and the expected SGWB spectrum. We present our constraint procedure as well as our derived abundance constraints in Section 4; additionally, we report systematic tests on the effect of varying  $q_{\max}$ . Lastly, we discuss our conclusions and outlook in Section 5.

## 2 Source and detector models

### 2.1 Parameter initialization and GW waveforms

All parameter initialization and source-detector simulations are facilitated with the use of Python package `gwent` [29]. For detectors, we chose to simulate the LISA L3 proposal [30] and the Einstein Telescope (ET) design proposal D [31]. This choice of detectors allow us to cover at least four decades of the GW frequency band. Figure 1 shows the sensitivity curves for both LISA and ET (orange and blue curves, respectively).

For resolvable PBH binary sources, we cover the full range of total binary masses  $M_{\text{tot}} = M_1 + M_2$  detectable by LISA and ET, respectively, namely:  $M_{\text{tot}} = 1\text{--}10^9 M_{\odot}$  for LISA and  $M_{\text{tot}} = 10^{-6}\text{--}10^6 M_{\odot}$  for ET. Contributions from binaries with  $M_{\text{tot}}$  outside these ranges are treated as negligible, as they have insignificant contribution to the SNR (as shown in Fig. 2 below). To include unresolved sources that fall within the SGWB window, we extend LISA’s range to  $M_{\text{tot}} = 10^{-6}\text{--}10^9 M_{\odot}$  in the case of the SGWB constraints. We also assume that the sources have no spin, i.e., set the component spin parameters  $\chi_1$  and  $\chi_2$  to zero, in line with the assumption that all PBHs form from almost perfectly spherically symmetric density peaks<sup>1</sup> [33].

The GW waveform package typically employed in PBH studies is IMRPhenomD [34, 35], which models black hole binaries with non-precessing spins up to a maximum mass ratio of  $q_{\max} = 18$ . The reasons for its ubiquity are twofold: most present PBH merger studies only deal with monochromatic sources with symmetric binaries ( $q = 1$ ), and the package has a Python implementation `pyIMRPhenomD` [36] which significantly optimizes calculation for Python codes. Given our interest in modeling extended mass distributions, we instead use IMRPhenomXAS as our waveform model. IMRPhenomXAS is also used for non-precessing black hole binaries, but it is also stated as an improvement over IMRPhenomD, covering mass ratios up to  $q_{\max} = 1000$  [37].

In contrast to existing actual and projected constraints to PBH abundance from GW observations [26, 38], which assume narrow mass functions, essentially including only binaries with relatively low mass ratios ( $q \lesssim 10$ ), we consider power law mass functions with mass ranges allowed by the scope of validity of the IMRPhenomXAS waveform models and include systems with a range of binary mass ratios  $q = 1\text{--}1000$ , allowing us to probe the intermediate mass ratio inspiral (IMRI) regime of PBH mergers.

<sup>1</sup>This assumption does not necessarily hold for PBHs formed during a matter-dominated epoch. See Ref. [32] for further reading.

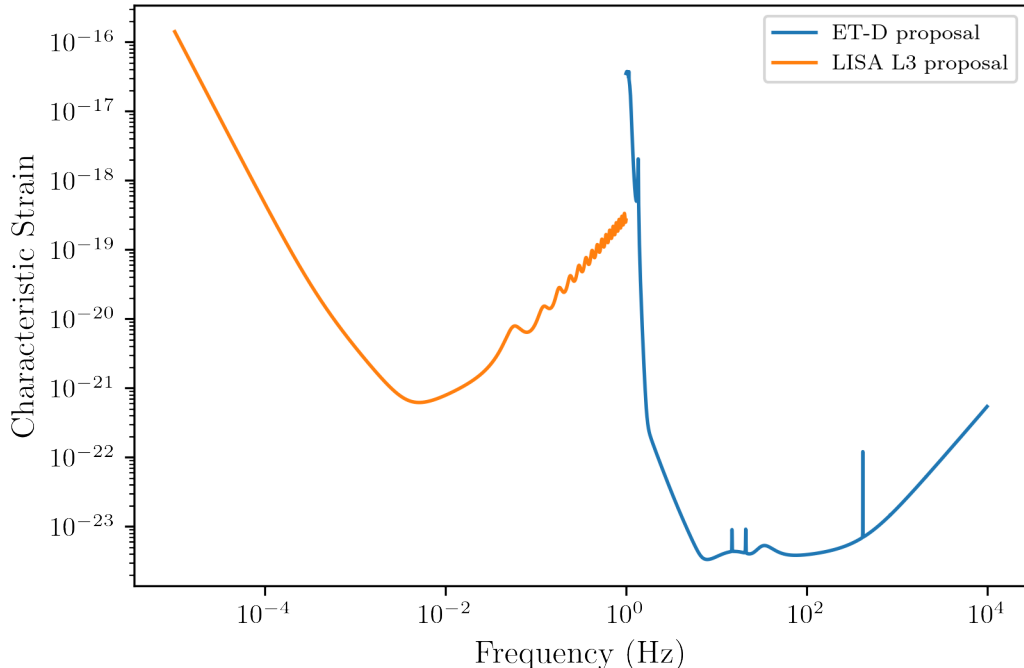


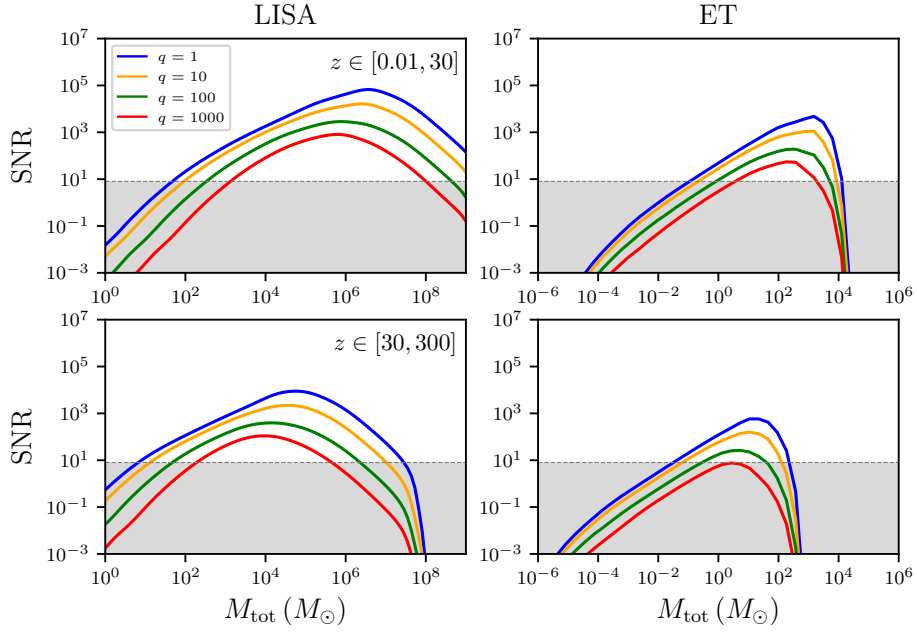
**Figure 1:** Proposed sensitivity curves for the Einstein Telescope [31] and LISA [30], based off existing design proposals.

## 2.2 Calculating detector SNR

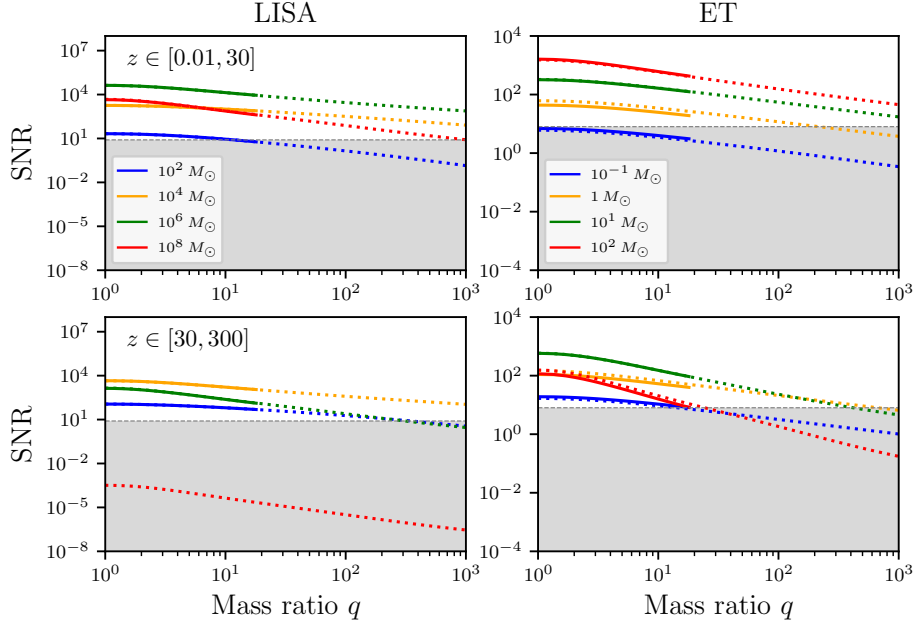
Detector SNR  $\rho_{\text{det}}$  is a function of source parameters (binary mass components, spin components, redshift), source waveform models (e.g., IMRPhenomD, IMRPhenomXAS), and detector sensitivity curves. The SNR calculation is also facilitated through the use of `gwent`. Source and detector parameters are as described above in Section 2.1. We calculate the SNR in a  $M_{\text{tot}} - q$  grid, integrating over a range of redshifts, from  $z = 0.01-30$  for the low-redshift range and from  $z = 30-300$  for the high-redshift range.

Figure 2 shows SNR curves for both LISA and ET detectors as a function of total mass  $M_{\text{tot}}$ , for fixed mass ratios  $q = 1, 10, 100,$  and  $10^3$ , for the low-redshift and high-redshift ranges (top and bottom panels, respectively). The shaded regions represent  $\text{SNR} \leq 8$ , lower than the threshold for a significant detection. These plots show the varying ranges in  $M_{\text{tot}}$  that LISA and ET can detect and justifies our choice of included mass ranges for the two detectors, as specified above in Sec. 2.1.

Additionally, Figure 3 shows SNR as a function of binary mass ratio  $q$  (dotted curves) for fixed total masses  $M_{\text{tot}} = 10^2, 10^4, 10^6$  and  $10^8 M_{\odot}$  for LISA (left panels) and  $M_{\text{tot}} = 10^{-1}, 1, 10,$  and  $100 M_{\odot}$  for ET (right panels), for the low-redshift and high-redshift ranges (top and bottom panels, respectively). Here, we have selected masses for illustration based on the respective mass windows of the detectors. The trend in SNR with varying total mass is consistent with the inverted U-shape of the mass window curves in Fig. 2, as expected. As another check, we also show the SNR curves calculated using the IMRPhenomD waveform, over the scope of its validity ( $q \leq 18$ ) (solid curves). As expected, the curves closely match the



**Figure 2:** Detector SNRs as a function of total mass  $M_{\text{tot}}$  for fixed mass ratios  $q = 1, 10, 100, 1000$ , integrated over low (top panels) and high (bottom panels) redshift ranges, for LISA (left panels) and ET (right panels). The shaded region represents  $\text{SNR} \leq 8$ , lower than the threshold for a significant detection.



**Figure 3:** Detector SNRs as a function of binary mass ratio  $q$  for fixed total masses  $M_{\text{tot}} = 10^2, 10^4, 10^6$  and  $10^8 M_{\odot}$  for LISA (left panels) and  $M_{\text{tot}} = 10^{-1}, 1, 10, 100 M_{\odot}$  for ET (right panels), integrated over low (top panels) and high (bottom panels) redshift ranges. Solid curves show SNR curves for IMRPhenomD waveforms (up to  $q_{\text{max}} = 18$ ), while dotted curves show SNR for IMRPhenomXAS waveforms (up to  $q_{\text{max}} = 10^3$ ). The shaded region represents  $\text{SNR} \leq 8$ , lower than the threshold for a significant detection.

extended curves (using the IMRPhenomXAS waveform) over the regime where they overlap— with the exception of the SNR curve for  $M_{\text{tot}} = 10^8 M_{\odot}$  at high redshift, where the SNR using the IMRPhenomD waveform is much lower (not shown in the plot); both curves fall well below the SNR threshold.

### 2.3 Mass distributions

In this work, we consider bounded power law PBH mass distributions as well as monochromatic distributions for baseline comparison. While there are various choices for the normalization of the mass function, we choose to set  $\int \psi(M) dM = 1$ , such that  $\psi(M)$  has units of  $[M_{\odot}^{-1}]$ . We also define mass-averaged quantities  $\langle X(M) \rangle$ , following Ref. [39], as

$$\langle X(M) \rangle = \frac{\int dM \psi(M) X M^{-1}}{\int dM \psi(M) M^{-1}}. \quad (2.1)$$

In particular, the calculations for the reference mass  $M_c \equiv \langle M \rangle$  and  $\langle M^2 \rangle$  follow from this definition.

#### 2.3.1 Monochromatic mass distribution

The monochromatic mass distribution is simply defined by the Dirac delta distribution

$$\psi_{\text{mono}}(M; M_c) = \delta_D(M - M_c), \quad (2.2)$$

where  $M_c$  is the central mass of the distribution. This distribution is considered primarily as a simplification, and is useful when considering symmetric mass binary GW sources. Trivially, the average mass and average squared mass of this distribution are just  $\langle M \rangle = M_c$  and  $\langle M^2 \rangle = M_c^2$ , respectively.

#### 2.3.2 Bounded power law mass distribution

The bounded power law mass distribution is given by [19]:

$$\psi_{\text{PL}}(M; M_{\text{min}}, M_{\text{max}}, \gamma) = \begin{cases} \mathcal{N}_{\text{PL}} M^{\gamma-1}, & \text{when } M \in [M_{\text{min}}, M_{\text{max}}], \\ 0, & \text{otherwise,} \end{cases} \quad (2.3)$$

where  $\mathcal{N}_{\text{PL}}$  is the normalization factor given by

$$\mathcal{N}_{\text{PL}} = \begin{cases} \frac{\gamma}{M_{\text{max}}^{\gamma} - M_{\text{min}}^{\gamma}}, & \gamma \neq 0 \\ \frac{1}{\log(M_{\text{max}}/M_{\text{min}})}, & \gamma = 0. \end{cases} \quad (2.4)$$

Here,  $M_{\text{min}}$  and  $M_{\text{max}}$  are the minimum and maximum mass cut-offs of the distribution, and are related to each other by  $q_{\text{max}} = M_{\text{max}}/M_{\text{min}}$ , i.e., the maximum possible mass ratio for that distribution. As noted in Sec. 2.1, we set  $q_{\text{max}} = 1000$  based on the scope of validity of our assumed waveform model. Later in Sec. 4.4, we investigate the effect of varying  $q_{\text{max}}$  on our derived PBH abundance constraints. The exponent  $\gamma$  relates to the cosmological equation of state during the PBH formation epoch [40]. A power law mass distribution is also formulated by Ref. [41], which sets the exponent at  $\gamma = -1/2$ . This particular form of the mass distribution arises from assuming that collapsing primordial fluctuations form a broad and flat power spectrum in  $k$ -space.

$ \gamma $	$\sigma_{\text{PBH}}$		
	$q_{\text{max}} = 10$	$q_{\text{max}} = 100$	$q_{\text{max}} = 1000$
10	0.1005	0.1005	0.1005
1	0.6381	1.1615	1.5687
0.1	0.7255	1.8911	4.3926
0.01	0.7265	1.9029	4.4619
0	0.7265	1.9030	4.4626

**Table 1:**  $\sigma_{\text{PBH}}$  for selected values of  $|\gamma|$  at different  $q_{\text{max}}$ , up to four decimal places.

From Eq. 2.1, we may compute for  $\langle M \rangle$  and  $\langle M^2 \rangle$  for this bounded power law distribution. We find that

$$M_c \equiv \langle M \rangle = \begin{cases} \frac{q_{\text{max}}-1}{\log q_{\text{max}}} M_{\text{min}}, & \gamma = 1, \\ \frac{q_{\text{max}} \log q_{\text{max}}}{q_{\text{max}}-1} M_{\text{min}}, & \gamma = 0, \\ \frac{\gamma-1}{\gamma} \frac{q_{\text{max}}-1}{q_{\text{max}}-1} M_{\text{min}}, & \text{otherwise,} \end{cases} \quad (2.5)$$

where we have reduced the general expression for the special cases,  $\gamma = 0$  and 1. Similarly, we find that  $\langle M^2 \rangle$  is given by

$$\langle M^2 \rangle = \begin{cases} \frac{q_{\text{max}}^2-1}{2 \log q_{\text{max}}} M_{\text{min}}^2, & \gamma = 1, \\ \frac{2q_{\text{max}}^2 \log q_{\text{max}}}{q_{\text{max}}^2-1} M_{\text{min}}^2, & \gamma = -1, \\ \frac{\gamma-1}{\gamma+1} \frac{q_{\text{max}}^{\gamma+1}-1}{q_{\text{max}}-1} M_{\text{min}}^2, & \text{otherwise,} \end{cases} \quad (2.6)$$

where we have reduced the general expression for the special cases,  $\gamma = -1$  and 1.

Any mass distribution can be characterized by a dimensionless width parameter  $\sigma_{\text{PBH}}$  characterizing the spread of the distribution, given by  $\sigma_{\text{PBH}}^2 = (\langle M^2 \rangle / \langle M \rangle^2) - 1$ . For the case of the bounded power law distribution defined in Eq. 2.3, the width  $\sigma_{\text{PBH}}$  simply depends on  $|\gamma|$  and  $q_{\text{max}}$ . Table 1 lists values of  $\sigma_{\text{PBH}}$  for selected values of  $|\gamma|$  and  $q_{\text{max}}$ , for reference. We note that  $\sigma_{\text{PBH}}$  attains its largest value when  $\gamma = 0$ , given by

$$\sigma_{\text{PBH}}^2 = \frac{(q_{\text{max}} - 1)^2}{q_{\text{max}} \log^2 q_{\text{max}}} - 1. \quad (2.7)$$

For our chosen value of  $q_{\text{max}} = 1000$ ,  $\sigma_{\text{PBH},\gamma=0} \approx 4.46$ . Another special case is for  $\gamma = \pm 1$ , where the expression reduces to

$$\sigma_{\text{PBH}}^2 = \frac{\log q_{\text{max}}}{2} \left( \frac{q_{\text{max}} + 1}{q_{\text{max}} - 1} \right) - 1. \quad (2.8)$$

For our chosen value of  $q_{\text{max}} = 1000$ ,  $\sigma_{\text{PBH},\gamma=\pm 1} \approx 1.57$ . For  $|\gamma| < 1$ ,  $\sigma_{\text{PBH}}$  ranges from  $\sigma_{\text{PBH},\gamma=\pm 1}$  to  $\sigma_{\text{PBH},\gamma=0}$ . On the other hand, for  $|\gamma| > 1$ ,  $\sigma_{\text{PBH}} < \sigma_{\text{PBH},\gamma=\pm 1}$  and approaches zero as  $|\gamma| \rightarrow \infty$ , reducing to the monochromatic case.

### 3 Calculating the constraining observables

#### 3.1 Expected detectable merger event rate

For resolvable PBH mergers, the expected number of merger events per year  $N_{\text{det}}$  is given by [23, 42]

$$N_{\text{det}} = \int dz dM_1 dM_2 \frac{1}{1+z} \frac{dV_c(z)}{dz} \frac{d^2 R_{\text{PBH}}}{dM_1 dM_2} p_{\text{det}}(M_1, M_2, z). \quad (3.1)$$

Here,  $V_c(z)$  is the comoving volume per unit redshift, and  $p_{\text{det}}$  is the binary detectability of any mass pair  $M_1$  and  $M_2$  at a redshift  $z$  for some particular GW detector, and  $R_{\text{PBH}}$  is the differential PBH merger rate.  $p_{\text{det}}$  is determined by the ratio between the optimal detector signal-to-noise ratio (SNR)  $\rho_{\text{det}}$  and a preset detection threshold  $\rho_{\text{thr}}$ , which we set to be equal to 8. We use the form of  $p_{\text{det}}$  as described in the Appendix of [42] for a single detector.

The differential PBH merger rate  $R_{\text{PBH}}$  is given by [23, 43, 44]

$$\frac{d^2 R_{\text{PBH}}}{dM_1 dM_2} = \frac{1.6 \times 10^6}{\text{Gpc}^3 \text{ yr}} f_{\text{PBH}}^{53/37} \eta^{-34/37} \left(\frac{t}{t_0}\right)^{-34/37} \left(\frac{M_{\text{tot}}}{M_{\odot}}\right)^{-32/37} \times \\ \times S(M_1, M_2, f_{\text{PBH}}, t) \psi(M_1) \psi(M_2), \quad (3.2)$$

where  $M_1$  and  $M_2$  are the principal masses of the PBH binary,  $M_{\text{tot}} = M_1 + M_2$  is the initial total mass of the binary upon formation,  $\eta = (M_1 M_2) / M_{\text{tot}}^2$  is the symmetric mass ratio of the binary,  $\psi(M)$  denotes the PBH mass distribution upon formation, and the suppression factor  $S = S_1 \times S_2$ , where  $S_1$  accounts for disruption due to inhomogeneities in the DM fluid and neighboring PBHs and  $S_2$  accounts for disruption due to substructures forming later in the Universe. We discuss each of these factors below.

An exact expression for the first suppression factor  $S_1$  is given by Eq. 2.37 in Ref. [45] for extended mass functions. Ref. [24] gives an approximation which we adopt here for efficient computation, given by

$$S_1 \approx 1.42 \left[ \frac{\sigma_{\text{PBH}}^2 + 1}{\bar{N}(y) + C} + \frac{\sigma_M^2}{f_{\text{PBH}}^2} \right]^{-21/74} e^{-\bar{N}(y)}, \quad (3.3)$$

where  $\sigma_{\text{PBH}}^2$  is the variance characterizing the spread of the PBH mass function (introduced in Sec. 2.3.2) and  $\sigma_M^2$  is the rescaled variance of matter density perturbations at the time of formation of the binary, approximately equal to  $3.6 \times 10^{-5}$ . Here,  $y$  is the minimal distance to the next-nearest-neighbor (i.e., third PBH) and  $\bar{N}(y)$  is the expected number of PBHs within a sphere of comoving radius  $y$  around the initial PBH pair, estimated as

$$\bar{N}(y) = \frac{M_{\text{tot}}}{\langle M \rangle} \frac{f_{\text{PBH}}}{f_{\text{PBH}} + \sigma_M}, \quad (3.4)$$

and  $C$  is a fitting parameter written out as

$$C(f_{\text{PBH}}, \sigma_{\text{PBH}}) = f_{\text{PBH}}^2 \frac{\sigma_{\text{PBH}}^2 + 1}{\sigma_M^2} \left\{ \left[ \frac{\Gamma(29/37)}{\sqrt{\pi}} U \left( \frac{21}{74}, \frac{1}{2}, \frac{5f_{\text{PBH}}^2}{6\sigma_M^2} \right) \right]^{-74/21} - 1 \right\}^{-1}, \quad (3.5)$$

where  $U$  is the confluent hypergeometric function. We note that while this approximation is accurate to within 7% for log-normal mass functions with widths  $\sigma \leq 2$  according to Ref. [24], for the bounded power law distributions we study here, the deviations from the exact expression can generally be larger, albeit still acceptable for the parameter ranges of interest; we find that the deviation increases with increasing  $\gamma$  and decreasing  $M_{\text{tot}}$ . Specifically, for  $\gamma = 10$  (the highest value we consider) and  $M_{\text{tot}} = 10^{-1} M_{\odot}$ , the percent difference ranges from around 20–45% for  $f_{\text{PBH}}$  from  $10^{-4}$  to  $10^{-3}$  and increases with  $f_{\text{PBH}}$  to around 50% for  $f_{\text{PBH}} \gtrsim 10^{-2}$ .

The second suppression factor  $S_2$  accounts for PBH-binary scattering within DM structures (haloes/subhaloes) and an estimate was derived in Ref. [46] for a monochromatic mass



distribution. For a given redshift of the merger, the value of  $S_2$  depends only on  $f_{\text{PBH}}$ , and is equal to 1 for  $f_{\text{PBH}}$  values up to some threshold value that depends on the redshift. For  $z = 0$ , this threshold value attains its lowest value, around 0.003; it increases to around 0.03 for  $z = 30$  and to around 0.1 for  $z = 300$ . In general, the impact of  $S_2$  is not expected to be significant when  $f_{\text{PBH}}$  is low, as the probability of disruption is also lower. As far as we know, an expression valid for extended mass distributions is not yet available in the literature and investigating this could be the scope of future work. In this work, we have simply set  $S_2 = 1$ .

Note that the calculation of the expected event rate  $N_{\text{det}}$  involves both an integration across not just a redshift range but also across a mass range. For monochromatic PBH mass distributions, this mass range collapses to  $M_c$ ; all detectable PBH merger events associated with the reference mass  $M_c$  are due to binaries of total mass with the same order of magnitude as the reference mass ( $M_{\text{tot}} = 2M_c$ )<sup>2</sup>. However, this is not the case for broad mass distributions such as power law. Instead, each event rate attributed to a power law distribution  $\psi$  with parameters  $M_c$  and  $\gamma$  contains the integrated contribution of all binaries with component masses within the range of  $M_{\text{min}}$  to  $M_{\text{max}}$  sampled from  $\psi$ . We note that because of how the mass range bounds are defined in Sec. 2.3, the resulting integration bounds in Eq. (3.1) may technically include binaries with total masses outside the detection ranges we have set for LISA and ET in Sec. 2.1; in practice, we do not include these contributions for simplicity, as they are expected to be negligible.

### 3.2 Expected stochastic GW background

For a merging population of compact binary objects, with component masses  $M_1$  and  $M_2$ , the generic expression for the expected SGWB spectrum at frequency  $\nu$  is given by [47, 48]

$$\Omega_{\text{GW}}(\nu) = \frac{\nu}{\rho_0} \int_0^{\frac{\nu_{\text{cutoff}}}{\nu} - 1} dz dM_1 dM_2 \frac{1}{(1+z)H(z)} \frac{d^2 R}{dM_1 dM_2} \frac{dE_{\text{GW}}(\nu_S)}{d\nu_S}, \quad (3.6)$$

where the present energy density  $\rho_0 = 3H_0^2 c^2 / 8\pi G$ ,  $H_0$  is the Hubble constant,  $H(z)$  is the Hubble parameter at redshift  $z$ ,  $R$  is the differential merger rate, and  $E_{\text{GW}}$  is the energy spectrum of GWs from the binary black hole (BBH) mergers. Note that the redshift integration is done up to  $z_{\text{cutoff}} = (\nu_{\text{cutoff}}/\nu) - 1$ . We are interested in calculating Eq. 3.6 for PBH binary mergers, i.e., for  $R = R_{\text{PBH}}$  given in Eq. 3.2. We assume a  $\Lambda$ CDM cosmology with  $h = 0.7$ ,  $\Omega_m = 0.3$ , and  $\Omega_{\text{de}} = 0.7$ .

The energy spectrum of GWs from BBH mergers is given by a phenomenological formulation of  $E_{\text{GW}}$  in terms of the redshifted source frequency  $\nu_S = \nu(1+z)$ . We lay out here the full form of  $E_{\text{GW}}$  formulated in Ref. [49], utilizing the non-spinning ( $\chi_1 = \chi_2 = 0$ ) limit:

$$\frac{dE_{\text{GW}}(\nu)}{d\nu} = \frac{(\pi G)^{2/3} M_{\text{tot}}^{5/3} \eta}{3} \begin{cases} \nu^{-1/3} (1 + \alpha_2 \bar{\nu}^2)^2, & \text{if } \nu < \nu_{\text{merg}}, \\ w_1 \nu^{2/3} (1 + \epsilon_1 \bar{\nu} + \epsilon_2 \bar{\nu}^2)^2, & \text{if } \nu_{\text{merg}} \leq \nu < \nu_{\text{ring}}, \\ w_2 \nu^2 [\mathcal{L}(\nu, \nu_{\text{ring}}, \varsigma)]^2, & \text{if } \nu_{\text{ring}} \leq \nu < \nu_{\text{cutoff}}, \end{cases} \quad (3.7)$$

where  $\bar{\nu} = (\pi G M_{\text{tot}} \nu / c^3)^{1/3}$ ,  $\alpha_2 = (451/168)\eta - 323/224$ ,  $\epsilon_1 = -1.8897$ , and  $\epsilon_2 = 1.6557$ .

<sup>2</sup>We infer that the same can be said for narrowly-peaked lognormal mass distributions, as the probability of drawing a component mass much smaller or larger than  $M_c$  falls off quite fast, reducing its weight towards the total integration.

The continuity constants  $w_i$  connecting the different frequency regimes are given by

$$\begin{aligned} w_1 &= \nu_{\text{merg}}^{-1} \frac{(1 + \alpha_2 \bar{\nu}_{\text{merg}}^2)^2}{(1 + \epsilon_1 \bar{\nu}_{\text{merg}}^1 + \epsilon_2 \bar{\nu}_{\text{merg}}^2)^2} \\ w_2 &= w_1 \nu_{\text{ring}}^{-4/3} (1 + \epsilon_1 \bar{\nu}_{\text{ring}}^1 + \epsilon_2 \bar{\nu}_{\text{ring}}^2)^2, \end{aligned} \quad (3.8)$$

where  $\bar{\nu}_i = (\pi G M_{\text{tot}} \nu_i / c^3)^{1/3}$ , and the frequencies  $\nu_i = \{\nu_{\text{merg}}, \nu_{\text{ring}}, \nu_{\text{cutoff}}, \varsigma\}$  are the merger, ringdown, and cutoff frequencies respectively of a BBH with parameters  $M_{\text{tot}}$  and  $\eta$  for some specific waveform model, while  $\varsigma$  is the width of the Lorentzian distribution  $\mathcal{L}$ . Writing out these frequencies, we obtain

$$\begin{aligned} \bar{\nu}_{\text{merg}} &= (1 - 4.455 + 3.521) + 0.6437\eta - 0.05822\eta^2 - 7.092\eta^3, \\ \bar{\nu}_{\text{ring}} &= (1 - 0.63)/2 + 0.1469\eta - 0.0249\eta^2 + 2.325\eta^3, \\ \pi G M_{\text{tot}} \varsigma / c^3 &= (1 - 0.63)/4 - 0.4098\eta + 1.829\eta^2 - 2.87\eta^3, \\ \bar{\nu}_{\text{cutoff}} &= 0.3236 - 0.1331\eta - 0.2714\eta^2 + 4.922\eta^3. \end{aligned} \quad (3.9)$$

In order to derive constraints on  $f_{\text{PBH}}$ , we need to set a detection threshold. Following [50], we calculate the SNR for SGWB detection from

$$\rho_{\text{det}} = \sqrt{\mathcal{T} \int_{\nu_{\text{min}}}^{\nu_{\text{max}}} d\nu \left( \frac{\Omega_{\text{GW}}(\nu)}{\Omega_{\text{sens}}(\nu)} \right)^2}, \quad (3.10)$$

where  $\Omega_{\text{sens}}(\nu)$  is the dimensionless energy in noise of the detector,  $\mathcal{T} = 1 \text{ yr}$  is the target observation period, and the limits of integration  $[\nu_{\text{min}}, \nu_{\text{max}}]$  define the bandwidth of the detector. Here, we set our SNR threshold to be  $\rho_{\text{thr}} = 5$  and consider SGWB detection if  $\rho_{\text{det}} \geq \rho_{\text{thr}}$ .

Finally, we note that we have adopted the approximation in Eq. 3.7 and applied it to our calculations involving binaries with mass ratios up to  $q_{\text{max}} = 1000$ , even though Ref. [49] notes that it is recommended only for modeling mergers up to mass ratios  $q_{\text{max}} \lesssim 10$ , given limitations in the numerical relativity calculations performed by the authors. In Sec. 4.4, we present how our derived constraints on PBH abundance vary with the choice of  $q_{\text{max}}$ .

## 4 Constraints on PBH abundance

### 4.1 Methodology

Before we present our results on constraints on PBH abundance from resolvable mergers and the SGWB (in Secs. 4.2 and 4.3, respectively), we first summarize the parameters assumed in our SNR calculations in Table 2.

With these assumptions, we obtain constraints for monochromatic and bounded power law mass distributions (as described in Sec. 2.3.2), with selected values of the power-law exponent  $\gamma$ . For resolvable mergers, we consider selected values of  $\gamma$  within the range  $[-10, 10]$ , including  $\gamma = 0$ ; specifically, we defined 7 equally log-spaced values of  $|\gamma|$  (for a total of 15 values). For the SGWB, we consider 3 values of  $\gamma$ , equal to  $-1/2, 0, 1/2$ . We obtain constraints for a range of reference masses  $M_c$  equal to the range in total masses listed in Table 2. We note that for simplicity, initial spin, clustering, and accretion effects on the PBH merger rate are ignored.

	Resolvable mergers	SGWB
Binary mass detection range $M_{\text{tot}}$	LISA: $1\text{--}10^9 M_{\odot}$ ET: $10^{-6}\text{--}10^6 M_{\odot}$	LISA: $10^{-6}\text{--}10^9 M_{\odot}$ ET: $10^{-6}\text{--}10^6 M_{\odot}$
Binary mass ratios $q$	1 – 1000	1 – 1000
Binary component spins $\chi_1$ and $\chi_2$	0	0
Waveform model	IMRPhenomXAS	Eq. 3.7
Simulated observation time $\mathcal{T}$	1 yr	1 yr
Detection threshold $\rho_{\text{thr}}$	8	5

**Table 2:** Parameters assumed in the calculation of SNR for resolvable mergers and SGWB observations.

For the calculation of the  $f_{\text{PBH}}$  constraints from resolvable mergers, we first define a log-spaced grid in  $M_{\text{tot}}$  and a linearly-spaced grid in  $q$  and pre-calculate the SNR for each detector using `gwent` [29]; the ranges in  $q$  and  $M_{\text{tot}}$  (per detector) are as specified in Table 2. This results in a  $50 \times 50$   $M_{\text{tot}} - q$  SNR table per redshift, for 100 equal log-spaced bins from  $z = 0$  to 300. We do this for both LISA and ET, preparing a total of 100 SNR tables each.

We use these SNR values  $\rho_{\text{det}}$  to obtain  $p_{\text{det}}$  in Eq. (3.1) for a given combination of  $M_1$ ,  $M_2$ , and  $z$ . The bounds of mass integration are determined by  $M_{\text{min}}$  and  $M_{\text{max}}$ , and we assign  $q_{\text{max}} = 1000$  unless specified. The bounds for redshift integration are set to be  $z \in [0.01, 30]$  for low redshift events and  $z \in [30, 300]$  for high redshift events.

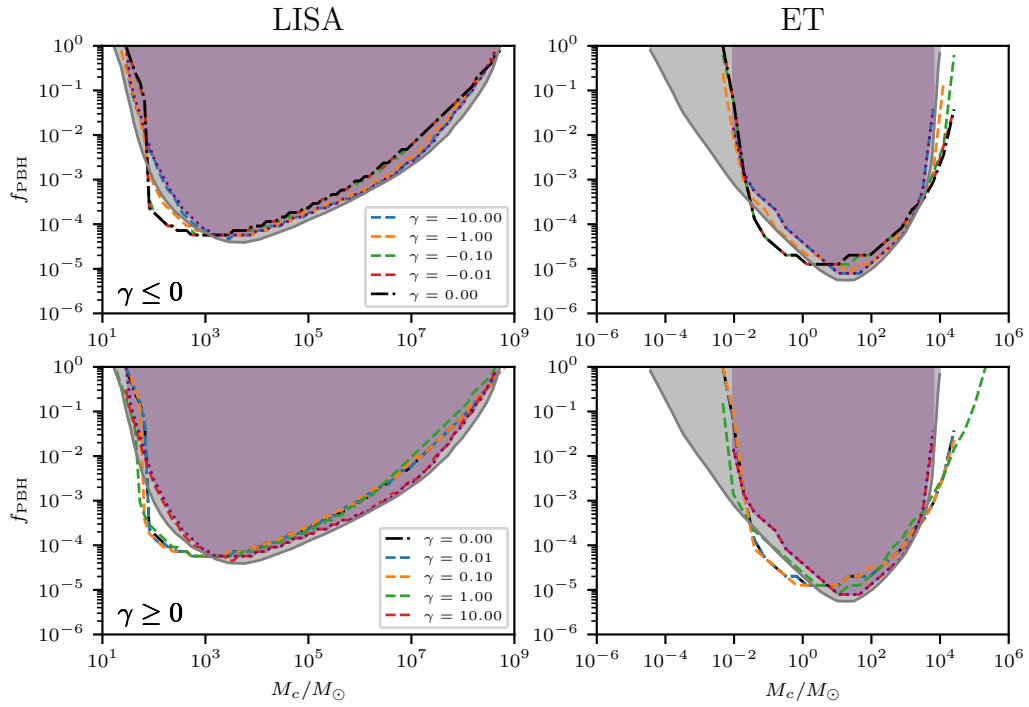
Next, we obtain the expected PBH integrated event rate  $N_{\text{det}}$  for each  $(M_c, \gamma, f_{\text{PBH}})$  point in the parameter space, where we choose 100 equal log-spaced bins in  $M_c$  for the specified range (per detector) and  $f_{\text{PBH}}$  runs from  $10^{-8}$  to 1 in 100 equal log-spaced bins.

Once all event rates within the parameter space have been calculated, we scan through the  $f_{\text{PBH}}$  range for each  $(M_c, \gamma)$  pair and pick the minimum  $f_{\text{PBH}}$  value where the expected event rate  $N_{\text{det}} \geq 1$ . These minimum  $f_{\text{PBH}}$  values serve as our constraint for a particular reference mass  $M_c$  and power law distribution.

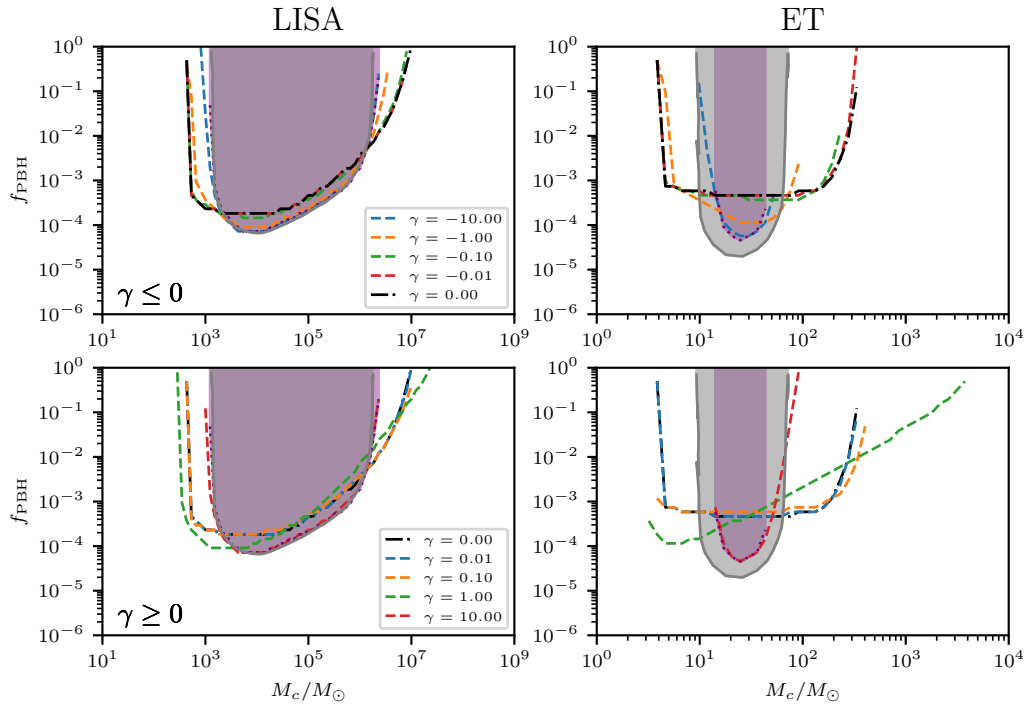
We follow a similar procedure to calculate constraints from the SGWB spectrum, going through each point in the  $(M_c, \gamma, f_{\text{PBH}})$  parameter space and calculating the expected SGWB spectrum using Eq. 3.6, then applying Eq. 3.10 to get the corresponding SNR,  $\rho_{\text{det}}$ . Finally, we choose the minimum  $f_{\text{PBH}}$  value where this is higher than the threshold value,  $\rho_{\text{det}} \geq \rho_{\text{thr}}$  (for a particular  $M_c$  and  $\gamma$ ).

## 4.2 Constraints from resolvable mergers

We now present the constraints on the minimum PBH abundance  $f_{\text{PBH}}$  from GW detections of resolvable mergers. Figures 4a & 4b show constraint curves as a function of reference mass  $M_c$  for bounded power law distributions with varying power-law exponents  $\gamma$ , for low and high redshift events, respectively. In both Figures, the left and right panels show projected constraints for LISA and ET, respectively, and the top and bottom panels show constraints for distributions with  $\gamma \leq 0$  and  $\gamma \geq 0$ , respectively. Constraints from monochromatic distributions are shown by the purple dotted lines and shaded regions for comparison. Finally, the solid gray regions show the monochromatic constraints obtained by Ref. [26]. We find good agreement between the two monochromatic results for LISA, though not for ET, which may be due to differences in assumptions, e.g., different choices in waveform model (IMRPhenomXAS in this work vs. IMRPhenomD in Ref. [26]).

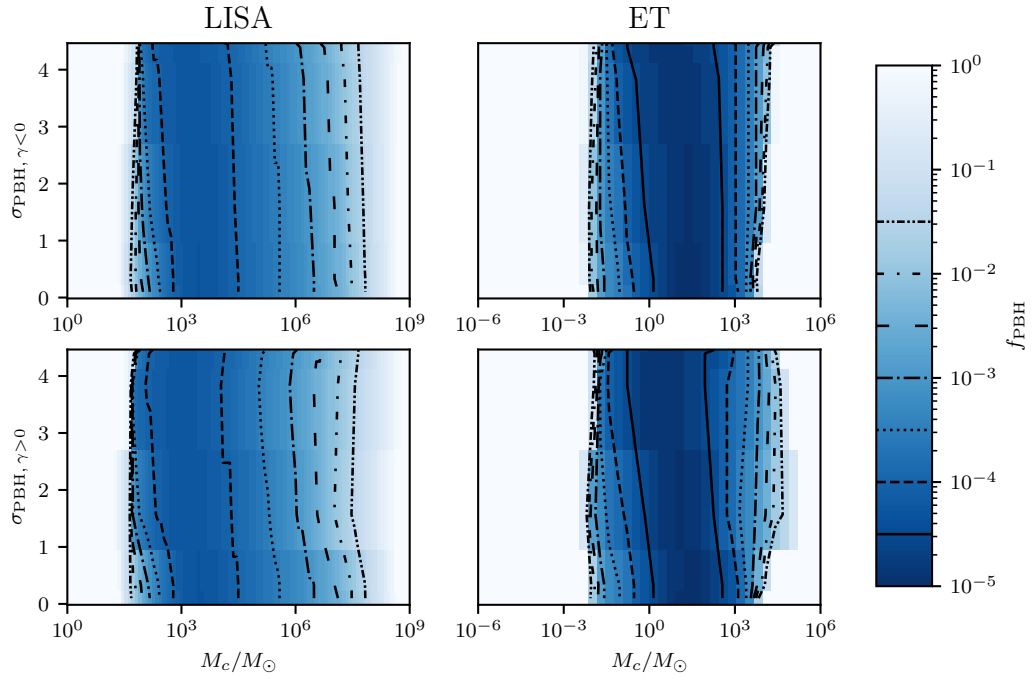


(a) Low-redshift events ( $z \in [0.01, 30]$ )

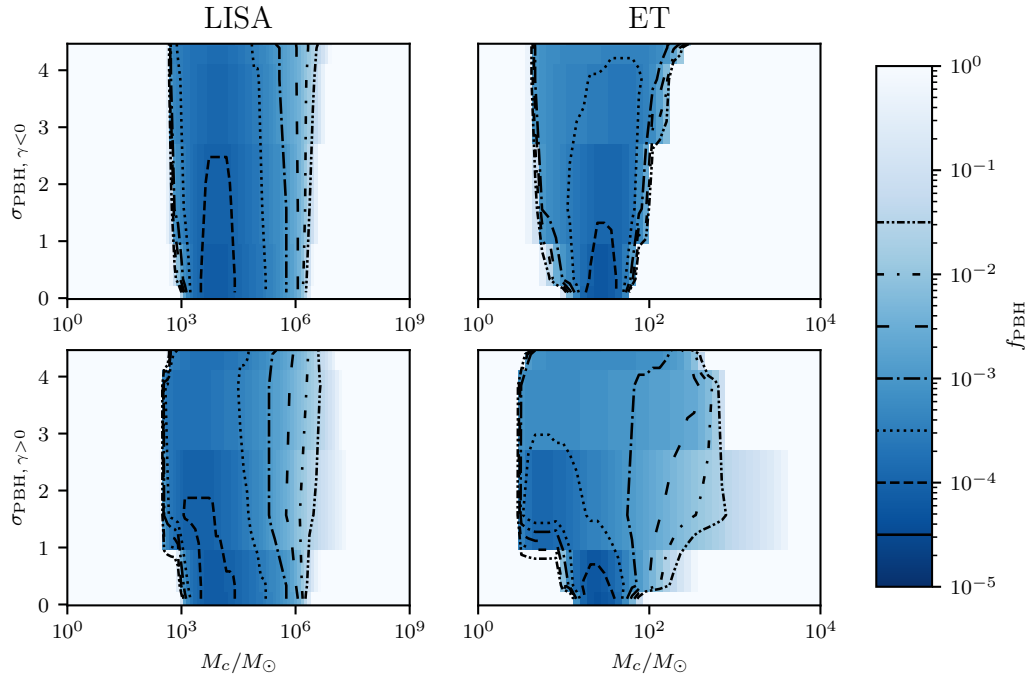


(b) High-redshift events ( $z \in [30, 300]$ )

**Figure 4:** Minimum PBH abundance  $f_{\text{PBH}}$  constraint curves for bounded power law distributions with varying power-law exponents  $\gamma$ , for selected values  $\gamma \leq 0$  (top panels) and  $\gamma \geq 0$  (bottom panels), for LISA (left panels) and ET (right panels). The purple regions show constraints derived for monochromatic distributions (using IMRPhenomXAS waveforms). For comparison, solid gray regions show the monochromatic constraints obtained by Ref. [26] (using IMRPhenomD waveforms).



(a) Low-redshift events ( $z \in [0.01, 30]$ )



(b) High-redshift events ( $z \in [30, 300]$ )

**Figure 5:**  $M_c - \sigma_{\text{PBH}}$  contour plots for LISA (left panels) and ET (right panels). Top panels show constraints for distributions with  $\gamma \leq 0$ , while bottom panels show constraints for  $\gamma \geq 0$ . Values of the  $f_{\text{PBH}}$  contours are indicated in the legend on the color bars. Unshaded white regions are classified as unconstrained by the detector (corresponding to  $f_{\text{PBH}} \geq 1$ ), while the darkest shades of blue signify regions of the parameter space with the lowest minimum PBH abundances.

As another way to visualize how these constraints vary with varying distribution profiles, Figures 5a & 5b show contour plots of  $f_{\text{PBH}}$  over the studied parameter space in  $M_c$  and  $\sigma_{\text{PBH}}$ . Recall that there is a one-to-one correspondence between the power-law exponent  $\gamma$  and the width of the distribution  $\sigma_{\text{PBH}}$  and for our choice of  $q_{\text{max}} = 1000$ , the maximum value of  $\sigma_{\text{PBH}}$  is around 4.46, corresponding to  $\gamma = 0$ , i.e., a top-hat distribution (c.f. Table 1). As in the previous set of Figures, the left and right panels show projected constraints for LISA and ET, respectively, and the top and bottom panels show constraints for distributions with  $\gamma \leq 0$  and  $\gamma \geq 0$ , respectively. Dark blue regions represent regions of the parameter space where there is an appreciably lower minimum abundance constraint (i.e.,  $f_{\text{PBH}} \lesssim 10^{-2}$ ), while the light blue regions correspond to regions where at least percent-level abundance is required to obtain a resolvable signal in one observation year. Regions colored white (unshaded) are classified as regions which require  $f_{\text{PBH}} \geq 1$ , i.e., unconstrained by the detector; in other words, the detector cannot set a physical constraint for a mass distribution within this region of the parameter space.

For the low-redshift events (Figs. 4a & 5a), the constraints for the minimum PBH abundance do not vary significantly from the monochromatic case for the extended mass distributions considered, for both LISA and ET. In contrast, for the high-redshift events (Figs. 4b & 5b), we find that the mass window generally broadens with smaller  $|\gamma|$  (higher  $\sigma_{\text{PBH}}$ ), corresponding to flatter (broader) distributions, for both LISA and ET. The minimum abundances generally become higher as well, up to one order of magnitude higher for ET at  $|\gamma| \sim 0$  compared to the monochromatic case. Meanwhile, for larger  $|\gamma|$  (lower  $\sigma_{\text{PBH}}$ ) values, the distributions approach a Dirac delta distribution, and the constraints approach the monochromatic case, as expected.

Figure 6 places our results in the context of existing constraints from the literature, which generally assume a monochromatic PBH mass distribution. Here, we show our derived constraints for ET (green) and LISA (red) for both monochromatic (solid) and top-hat (i.e.,  $\gamma = 0$ ) (dashed) distributions. This value of  $\gamma$  corresponds to the most contrasting departure from the monochromatic case. We compare these against constraints from gravitational-wave observations in the LIGO-Virgo-KAGRA (LVK) O3 run (GWO3) [25], Planck CMB measurements (assuming spherical and disk accretion) [15], dwarf galaxy dynamics (Segue I) [51] and heating (DGH) [52, 53], Lyman- $\alpha$  observations [18], X-ray binary observations (XRB) [54], dynamical friction (DF) [17], the neutron-to-proton ratio (n/p) [55], microlensing observations from Subaru HSC [7, 56], MACHO/EROS (E) [10, 57], OGLE (O) [6], and Icarus (I) [58], and CMB  $\mu$ -distortion [59], shown as the grey regions on the plots. We show the same regions on both low and high redshift plots for the sake of easy comparison, although we acknowledge that some of these constraints may be relaxed at high redshift. We note that each of these existing constraints have varying degrees of uncertainty and assumptions. In addition, these constraints are expected to change depending on the shape of the mass distribution considered [20].

We highlight that, as previously reported by Ref. [26], future GW observatories open a window to detect high-redshift PBHs, as illustrated in the right panel of Figure 6. These constraints exist even if the population at  $z < 30$ , which can be confused with an astrophysical BH population, is neglected, providing possible smoking-gun evidence for PBHs. LISA and ET observations would complement each other by probing different mass windows and this remains true for the case of extended mass distributions studied here.

At low redshift, ET projections generally lower the upper bound of abundance set by LVK GWO3. On the other hand, low-redshift LISA projections overlap with existing

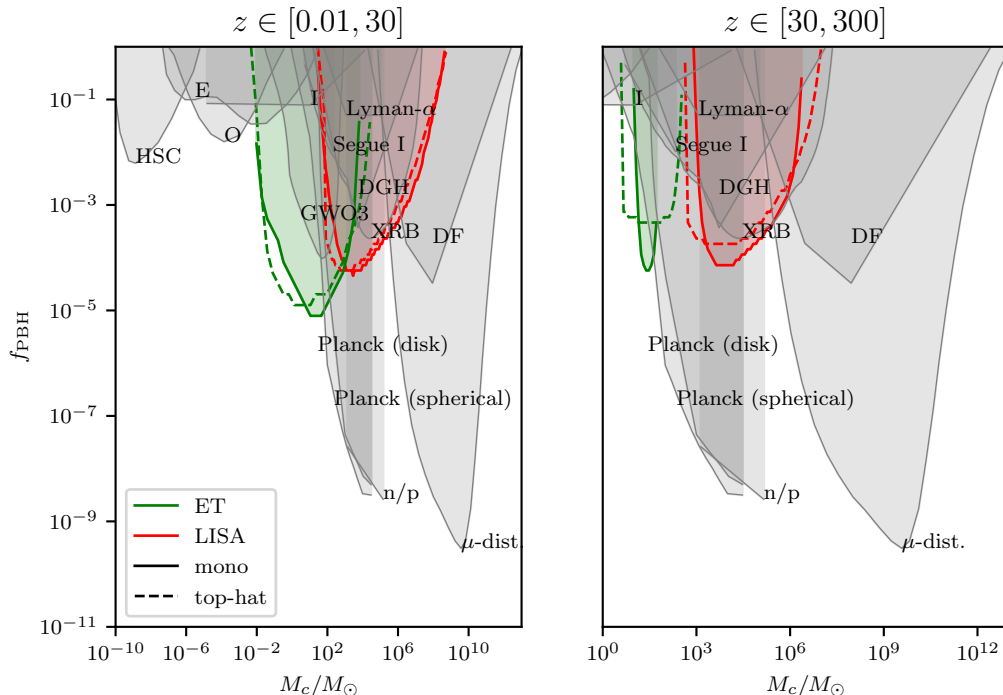


**Figure 6:** Projected  $f_{\text{PBH}}$  constraints for ET (green) and LISA (red) for monochromatic (solid) and top-hat (dashed) PBH mass distributions, from low- and high-redshift resolvable mergers (left and right panels, respectively), compared against existing present-day monochromatic constraints from the literature (solid curves, colored in grey). These include constraints from gravitational wave observations in the LVK O3 run (GWO3) [25] (shown in the left panel only), Planck CMB measurements [15], dwarf galaxy dynamics (Segue I) [51] and heating (DGH) [52, 53], Lyman- $\alpha$  observations [18], X-ray binary observations (XRB) [54], dynamical friction (DF) [17], the neutron-to-proton ratio (n/p) [55], microlensing observations from Subaru HSC [7, 56], MACHO/EROS (E) [10, 57], OGLE (O) [6], and Icarus (I) [58], as well as the CMB  $\mu$ -distortion [59]. Note that for the  $\mu$ -distortion constraint, we chose the FIRAS value corresponding to large non-Gaussianity ( $p = 0.5$ ).

constraints from local observations, particularly those coming from present-day constraints on PBH accretion (DGH, XRB) [52–54] and dynamical effects on dwarf galaxies (Segue I) [51]. These local constraints may potentially be relaxed at high redshift, or notably even disappear in the case of the LVK GWO3 constraints. However, going to high redshift does not let us evade constraints set by CMB  $\mu$ -distortion [15, 59] and BBN observations (“n/p”) [55], which most strongly constrain the region with  $M_c$  above  $10^2 M_\odot$ . We remark that even with a choice of a particularly conservative form of the  $\mu$ -distortion constraints (with non-Gaussianity parameter  $p = 0.5$ ), there is little to no room for PBHs of mass  $\sim 10^6 M_\odot$  at abundances  $f_{\text{PBH}} \sim 10^{-4}$ .

We note that Ref. [20] reports how the monochromatic constraints from the Segue I and Planck CMB shift for extended mass distributions, although these results are not shown here to avoid overcrowding the figures. Our contribution to the literature is to show how the monochromatic constraints from GW observations (as reported in e.g., Ref. [26]) are expected to shift for extended mass distributions.

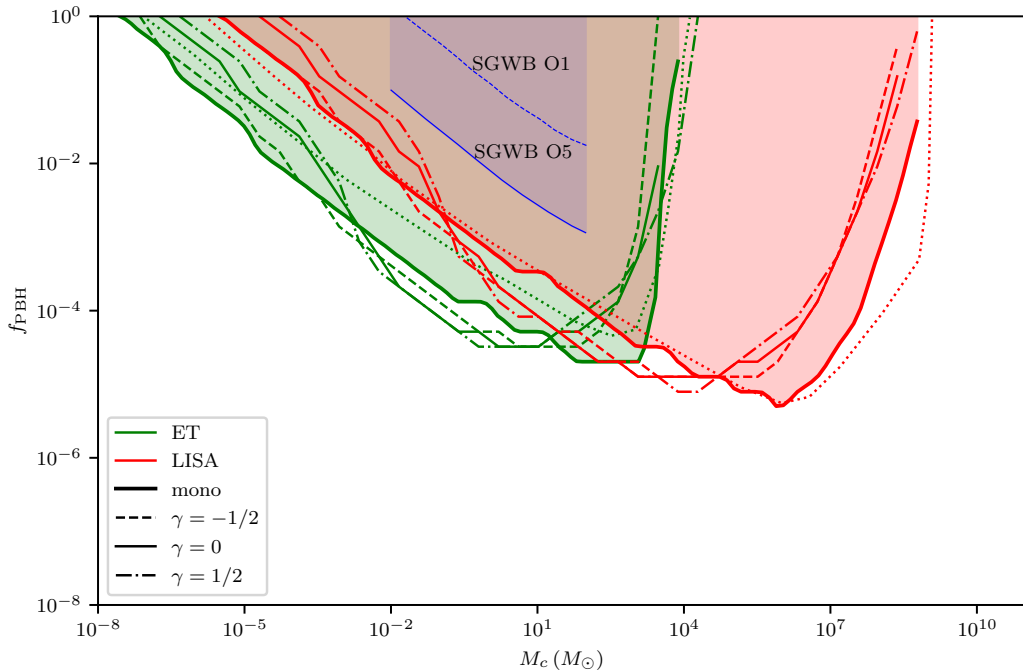


**Figure 7:** Minimum PBH abundance  $f_{\text{PBH}}$  constraint curves from SGWB for ET (green) and LISA (red) for monochromatic (thick solid) and top-hat (dashed) PBH mass distributions, compared against existing monochromatic constraints reported in Ref. [26] (dotted). Also shown are the existing LIGO O1 SGWB constraint (blue dotted curve, labeled SGWB O1) and the projected O5 SGWB constraint [60] (blue solid curve and region, labeled SGWB O5).

### 4.3 Constraints from SGWB

Next, we present the projected constraints on the minimum PBH abundance  $f_{\text{PBH}}$  from the unresolved SGWB. Figure 7 shows the constraint curves for ET and LISA (green and red curves, respectively), for the monochromatic case (thick solid) together with the top-hat (i.e.,  $\gamma = 0$ ) (thin solid) and bounded power-law distributions with  $\gamma = -1/2$  (dashed) and  $1/2$  (dot-dashed). We find that the constraints do not vary significantly for the extended distributions, except for a slight shift to the left compared to the monochromatic case, for both ET and LISA. Also shown for comparison are existing monochromatic constraints reported by Ref. [26] (dotted curves), which seem to match qualitatively although they may not match exactly because of a difference in assumptions, including in the selected SNR detection thresholds.

The planned detectors are expected to broaden the mass windows probed and lower the abundance constraints by around an order of magnitude for LISA and 2 orders for ET compared to the projected O5 SGWB constraint, which itself is an improvement of around an order of magnitude compared with the existing LIGO O1 SGWB constraint (both reported in Ref. [60]).



#### 4.4 Effect of varying maximum mass ratios

As noted in Sec. 2.1, in this work, we set the maximum mass ratio  $q_{\max} = 1000$  as constrained by the limits of the validity of our assumed waveform approximant, IMRPhenomXAS. As a test of systematics, we have checked how our derived constraints depend on the choice of maximum mass ratio  $q_{\max}$ . Varying this parameter modifies the value of the normalization of the mass function  $\mathcal{N}_{\text{PL}}$  (in Eq. 2.3), narrows the bounds of integration across the mass terms in the expected number of merger events  $N_{\text{det}}$  (in Eq. 3.2), and changes the value of the width parameter  $\sigma_{\text{PBH}}$  (consequently, affecting suppression factor  $S_1$ , given in Eq. 3.3).

We do these checks for the case of the top-hat PBH mass distribution ( $\gamma = 0$ ), which corresponds to the broadest profile studied and the largest value of  $\sigma_{\text{PBH}}$ . Figures 8 and 9 show the results for constraints from resolvable mergers and SGWB, respectively. These show that the broadening of the mass windows observed in the high-redshift merger events is robust to the choice of  $q_{\max}$  (lower panels of Fig. 8). Similarly, the slight shift in the left of the SWGB constraint curves is also consistently observed for lower  $q_{\max}$  values. Overall, these checks show that the main findings we have presented in the previous subsections are robust to the particular choice of  $q_{\max}$ .

## 5 Conclusions and outlook

In this paper, we set projected  $f_{\text{PBH}}$  abundance constraints from simulated LISA and ET observations for extended PBH mass distributions from both resolvable mergers and the SGWB. We achieved this by considering broad power law distributions for a range of negative and positive exponents  $\gamma$ , as well as top-hat distributions ( $\gamma = 0$ ), considering binary mergers with mass ratios up to  $q_{\max} = 1000$ , and modeling these resolvable mergers using IMRPhenomXAS waveforms. We find that the most significant impact of extended mass distributions is observed for the high-redshift merger events, for which the minimum abundances are elevated (i.e., constraints are looser) and the probed mass windows broaden compared to the case where the distribution is assumed to be monochromatic. For the low-redshift merger events and SGWB, the constraints are not significantly affected.

Our results also demonstrate that the ability of the future GW observatories to detect high-redshift GW mergers, where astrophysical BHs are not expected to contribute, is robust to the simplifying assumption of a monochromatic PBH mass distribution. LISA and ET observations would complement each other by probing different PBH mass windows and this remains true for the case of the extended mass distributions we investigated.

In this work, we have not yet properly included the impact of considering the suppression of the constraints from low-redshift merger events arising from an astrophysical foreground, and this can be the subject of future work. Bayesian analysis accounting for the combined PBH and astrophysical BH populations have been performed for ground-based detectors, e.g., in Refs. [61], [38], and [25], and extending this to future detectors would provide new and interesting insights.

Keeping assumptions about our PBH models constant, one way to evade the existing constraints is to have a detector that could probe at either higher sensitivities (reducing  $f_{\text{PBH}}$  necessary for a detection) or at higher mass ranges ( $M \gtrsim 10^{11} M_{\odot}$ ) across a wide range of redshifts. Setting aside the feasibility of such a detector, however, evading the  $\mu$ -distortion bound by simultaneously lowering the required abundance and raising the PBH mass would quickly run us into the incredulity limit, which sets the abundance lower bound for  $M \sim 10^{11} M_{\odot}$  at  $f_{\text{PBH}} \sim 10^{-10}$  [17].

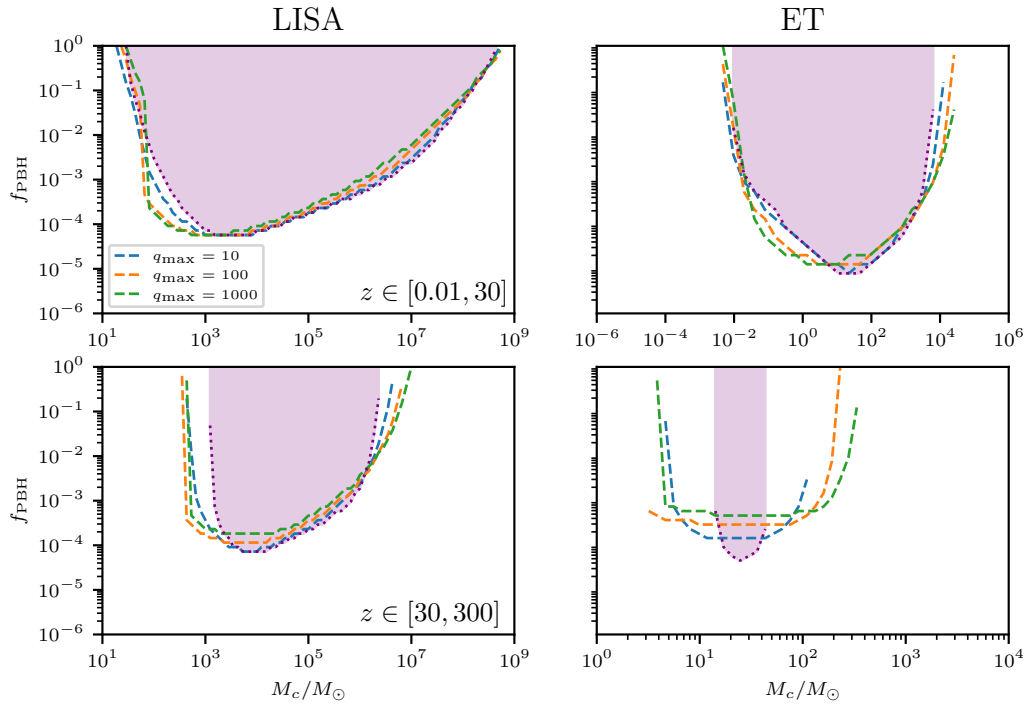


**Figure 8:** Minimum PBH abundance  $f_{\text{PBH}}$  constraint curves for LISA and ET (left and right panels) from low- and high-redshift events (top and bottom panels) assuming a top-hat distribution ( $\gamma = 0$ ) for different choices of the maximum mass ratio  $q_{\text{max}} = 10, 100, 1000$  (blue, orange, and green dashed curves, respectively). For comparison, the monochromatic cases are shown by the dotted purple curves and regions.

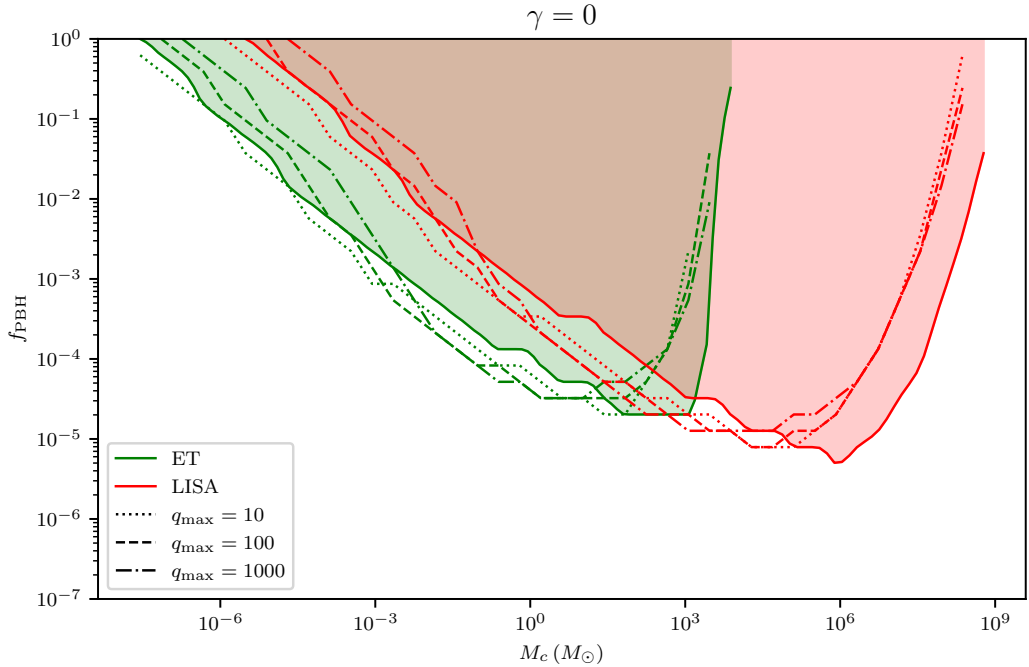


**Figure 9:** Minimum PBH abundance  $f_{\text{PBH}}$  constraint curves from SGWB for LISA (red) and ET (green) assuming a top-hat distribution ( $\gamma = 0$ ) for different choices of the maximum mass ratio  $q_{\text{max}} = 10, 100, 1000$  (dotted, dashed, and dot-dashed curves, respectively). For comparison, the monochromatic cases are shown by solid curves and regions.

There are other, less detector-dependent approaches to evading the existing constraints. Modifying the model to account for phenomenological uncertainties such as clustering [26, 62, 63] and accretion [64, 65] may also provide an avenue for evasion. Incorporating broadly extended mass distributions to these model additions may however introduce new uncertainties, such as the implications of an extended distribution to the initial clustering, as well as potential changes to the local PBH accretion environments as a result of strong initial clustering. Recent developments in excursion set methods to model PBH initial clustering [66] may allow for a more nuanced phenomenological description of the average neighbor count  $\bar{N}(y)$ , accounting not only for total mass  $M_{\text{tot}}$  and average mass  $\langle M \rangle$  but also the allowed mass ratios  $q$  of the distribution. Applying this formalism to concretely describe initial clustering for power law mass functions is non-trivial. However, if accomplished, it may lead to the development of PBH merger rate suppression factors that apply to a more general range of PBH mass functions.

Finally, we remark that broadly extended mass distributions may be relevant when considering the PBH merger rate of initially three-body configurations [46, 67]. This merger rate is considered subdominant to the two-body merger rate in the regime considered by LVK [25], but their analysis is restricted to narrow ( $\sigma \lesssim 1.2$ ) mass distributions. For these investigations, it would be interesting to consider even flatter and broader distributions. Generally, more work is needed in order to establish the nuance of how these very broad mass distributions affect the overall PBH merger rate.

## Acknowledgments

We would like to thank Gabriele Franciolini, Andrew Kaiser, and Reginald Bernardo for responding to our questions regarding parts of this manuscript, as well as the anonymous referee for their insightful comments. We acknowledge the use of Python package `gwent` [29] in the SNR and sensitivity curve computation for both LISA and ET.

## References

- [1] LIGO SCIENTIFIC COLLABORATION AND VIRGO COLLABORATION collaboration, *GWTC-2: Compact Binary Coalescences Observed by LIGO and Virgo during the First Half of the Third Observing Run*, *Phys. Rev. X* **11** (2021) 021053.
- [2] Z.C. Zhao and S. Wang, *Bayesian implications for the primordial black holes from NANOGrav’s pulsar-timing data using the scalar-induced gravitational waves*, *Universe* **9** (2023) .
- [3] A. Afzal, G. Agazie, A. Anumalapudi, A.M. Archibald, Z. Arzoumanian, P.T. Baker et al., *The NANOGrav 15 yr data set: Search for signals from new physics*, *Astrophys. J. Lett.* **951** (2023) L11.
- [4] B. Carr, K. Kohri, Y. Sendouda and J. Yokoyama, *Constraints on primordial black holes*, *Rep. Prog. Phys.* **84** (2021) 116902.
- [5] P. Villanueva-Domingo, O. Mena and S. Palomares-Ruiz, *A brief review on primordial black holes as dark matter*, *Front. Astron. Space Sci.* **8** (2021) 681084.
- [6] H. Niikura, M. Takada, S. Yokoyama, T. Sumi and S. Masaki, *Constraints on earth-mass primordial black holes from OGLE 5-year microlensing events*, *Phys. Rev. D* **99** (2019) 083503.
- [7] N. Smyth, S. Profumo, S. English, T. Jeltema, K. McKinnon and P. Guhathakurta, *Updated constraints on asteroid-mass primordial black holes as dark matter*, *Phys. Rev. D* **101** (2020) 063005.

- [8] K. Griest, A.M. Cieplak and M.J. Lehner, *New limits on primordial black hole dark matter from an analysis of Kepler source microlensing data*, *Phys. Rev. Lett.* **111** (2013) 181302.
- [9] K. Griest, A.M. Cieplak and M.J. Lehner, *Experimental limits on primordial black hole dark matter from the first 2 yr of Kepler data*, *Astrophys. J.* **786** (2014) 158.
- [10] C. Alcock, R.A. Allsman, D.R. Alves, T.S. Axelrod, A.C. Becker, D.P. Bennett et al., *MACHO project limits on black hole dark matter in the 1 – 30  $M_{\odot}$  range*, *Astrophys. J.* **550** (2001) L169.
- [11] M. Zumalacárregui and U. Seljak, *Limits on stellar-mass compact objects as dark matter from gravitational lensing of Type Ia supernovae*, *Phys. Rev. Lett.* **121** (2018) 141101.
- [12] A. Barnacka, J.-F. Glicenstein and R. Moderski, *New constraints on primordial black holes abundance from femtolensing of gamma-ray bursts*, *Phys. Rev. D* **86** (2012) 043001.
- [13] Tisserand, P., Le Guillou, L., Afonso, C., Albert, J. N., Andersen, J., Ansari, R. et al., *Limits on the MACHO content of the galactic halo from the EROS-2 survey of the magellanic clouds*, *A&A* **469** (2007) 387.
- [14] A.M. Green, *Microlensing and dynamical constraints on primordial black hole dark matter with an extended mass function*, *Phys. Rev. D* **94** (2016) 063530.
- [15] P.D. Serpico, V. Poulin, D. Inman and K. Kohri, *Cosmic microwave background bounds on primordial black holes including dark matter halo accretion*, *Phys. Rev. Res.* **2** (2020) 023204.
- [16] B.J. Carr and M. Sakellariadou, *Dynamical constraints on dark matter in compact objects*, *Astrophys. J.* **516** (1999) 195.
- [17] B. Carr and J. Silk, *Primordial black holes as generators of cosmic structures*, *MNRAS* **478** (2018) 3756  
[<https://academic.oup.com/mnras/article-pdf/478/3/3756/25077116/sty1204.pdf>].
- [18] R. Murgia, G. Scelfo, M. Viel and A. Raccanelli, *Lyman- $\alpha$  forest constraints on primordial black holes as dark matter*, *Phys. Rev. Lett.* **123** (2019) 071102.
- [19] N. Bellomo, J.L. Bernal, A. Raccanelli and L. Verde, *Primordial black holes as dark matter: converting constraints from monochromatic to extended mass distributions*, *J. Cosmol. Astropart. Phys.* **2018** (2018) 004.
- [20] B. Carr, M. Raidal, T. Tenkanen, V. Vaskonen and H. Veermäe, *Primordial black hole constraints for extended mass functions*, *Phys. Rev. D* **96** (2017) 023514.
- [21] F. Kühnel and K. Freese, *Constraints on Primordial Black Holes with Extended Mass Functions*, *Phys. Rev. D* **95** (2017) 083508 [1701.07223].
- [22] K.W.K. Wong, G. Franciolini, V. De Luca, V. Baibhav, E. Berti, P. Pani et al., *Constraining the primordial black hole scenario with bayesian inference and machine learning: The GWTC-2 gravitational wave catalog*, *Phys. Rev. D* **103** (2021) 023026.
- [23] M. Raidal, V. Vaskonen and H. Veermäe, *Gravitational waves from primordial black hole mergers*, *J. Cosmol. Astropart. Phys.* **2017** (2017) 037.
- [24] G. Hütsi, M. Raidal, V. Vaskonen and H. Veermäe, *Two populations of LIGO-Virgo black holes*, *J. Cosmol. Astropart. Phys.* **2021** (2021) 068.
- [25] M. Andrés-Carcasona, A.J. Iovino, V. Vaskonen, H. Veermäe, M. Martínez, O. Pujolàs et al., *Constraints on primordial black holes from ligo-virgo-kagra o3 events*, *Phys. Rev. D* **110** (2024) 023040.
- [26] V.D. Luca, G. Franciolini, P. Pani and A. Riotto, *The minimum testable abundance of primordial black holes at future gravitational-wave detectors*, *J. Cosmol. Astropart. Phys.* **2021** (2021) 039.

- [27] K.K.Y. Ng, G. Franciolini, E. Berti, P. Pani, A. Riotto and S. Vitale, *Constraining high-redshift stellar-mass primordial black holes with next-generation ground-based gravitational-wave detectors*, *Astrophys. J. Lett.* **933** (2022) L41.
- [28] G.L.A. Dizon and R. Reyes, *Role of extended mass distributions in minimum testable primordial black hole abundances from high-redshift mergers*, in *Proceedings of the Samahang Pisika ng Pilipinas*, vol. 40, (Legazpi, Philippines), pp. SPP-2022-1B-03, 2022.
- [29] A.R. Kaiser and S.T. McWilliams, *Sensitivity of present and future detectors across the black-hole binary gravitational wave spectrum*, *Class. Quantum Gravity* **38** (2021) 055009.
- [30] P. Amaro-Seoane, H. Audley, S. Babak, J. Baker, E. Barausse, P. Bender et al., *Laser Interferometer Space Antenna*, 2017. <https://doi.org/10.48550/arXiv.1702.00786>.
- [31] S. Hild, M. Abernathy, F. Acernese, P. Amaro-Seoane, N. Andersson, K. Arun et al., *Sensitivity studies for third-generation gravitational wave observatories*, *Class. Quant. Grav.* **28** (2011) 094013.
- [32] T. Harada, C.-M. Yoo, K. Kohri and K.-I. Nakao, *Spins of primordial black holes formed in the matter-dominated phase of the universe*, *Phys. Rev. D* **96** (2017) 083517.
- [33] T. Chiba and S. Yokoyama, *Spin distribution of primordial black holes*, *Prog. Theor. Phys.* **2017** (2017) 083E01 [<https://academic.oup.com/ptep/article-pdf/2017/8/083E01/19488901/ptx087.pdf>].
- [34] S. Husa, S. Khan, M. Hannam, M. Pürrer, F. Ohme, X.J. Forteza et al., *Frequency-domain gravitational waves from nonprecessing black-hole binaries. I. New numerical waveforms and anatomy of the signal*, *Phys. Rev. D* **93** (2016) 044006.
- [35] S. Khan, S. Husa, M. Hannam, F. Ohme, M. Pürrer, X.J. Forteza et al., *Frequency-domain gravitational waves from nonprecessing black-hole binaries. II. A phenomenological model for the advanced detector era*, *Phys. Rev. D* **93** (2016) 044007.
- [36] M.C. Digman and N.J. Cornish, *Parameter estimation for stellar-origin black hole mergers in lisa*, *Phys. Rev. D* **108** (2023) 023022.
- [37] G. Pratten, S. Husa, C. García-Quirós, M. Colleoni, A. Ramos-Buades, H. Estellés et al., *Setting the cornerstone for a family of models for gravitational waves from compact binaries: The dominant harmonic for nonprecessing quasicircular black holes*, *Phys. Rev. D* **102** (2020) 064001.
- [38] V.D. Luca, G. Franciolini, P. Pani and A. Riotto, *Primordial black holes confront ligo/virgo data: current situation*, *Journal of Cosmology and Astroparticle Physics* **2020** (2020) 044.
- [39] M. Raidal, V. Vaskonen and H. Veermäe, *Formation of primordial black hole binaries and their merger rates*, 2024.
- [40] B.J. Carr, *The primordial black hole mass spectrum*, *Astrophys. J.* **201** (1975) 1.
- [41] V. De Luca, G. Franciolini and A. Riotto, *On the primordial black hole mass function for broad spectra*, *Phys. Lett. B* **807** (2020) 135550.
- [42] M. Dominik, E. Berti, R. O’Shaughnessy, I. Mandel, K. Belczynski, C. Fryer et al., *Double compact objects. III. Gravitational-wave detection rates*, *Astrophys. J.* **806** (2015) 263.
- [43] T. Nakamura, M. Sasaki, T. Tanaka and K.S. Thorne, *Gravitational waves from coalescing black hole macho binaries*, *The Astrophysical Journal* **487** (1997) L139.
- [44] Y. Ali-Haïmoud, E.D. Kovetz and M. Kamionkowski, *Merger rate of primordial black-hole binaries*, *Phys. Rev. D* **96** (2017) 123523.
- [45] M. Raidal, C. Spethmann, V. Vaskonen and H. Veermäe, *Formation and evolution of primordial black hole binaries in the early universe*, *J. Cosmol. Astropart. Phys.* **2019** (2019) 018.

- [46] V. Vaskonen and H. Veermäe, *Lower bound on the primordial black hole merger rate*, *Phys. Rev. D* **101** (2020) 043015.
- [47] E.S. Phinney, *A practical theorem on gravitational wave backgrounds*, 2001.
- [48] X.-J. Zhu, E. Howell, T. Regimbau, D. Blair and Z.-H. Zhu, *Stochastic gravitational wave background from coalescing binary black holes*, *The Astrophysical Journal* **739** (2011) 86.
- [49] P. Ajith, M. Hannam, S. Husa, Y. Chen, B. Brügmann, N. Dorband et al., *Inspiral-merger-ringdown waveforms for black-hole binaries with nonprecessing spins*, *Phys. Rev. Lett.* **106** (2011) 241101.
- [50] E. Thrane and J.D. Romano, *Sensitivity curves for searches for gravitational-wave backgrounds*, *Phys. Rev. D* **88** (2013) 124032.
- [51] S.M. Koushiappas and A. Loeb, *Dynamics of dwarf galaxies disfavor stellar-mass black holes as dark matter*, *Phys. Rev. Lett.* **119** (2017) 041102.
- [52] P. Lu, V. Takhistov, G.B. Gelmini, K. Hayashi, Y. Inoue and A. Kusenko, *Constraining primordial black holes with dwarf galaxy heating*, *Astrophys. J. Lett.* **908** (2021) L23.
- [53] V. Takhistov, P. Lu, G.B. Gelmini, K. Hayashi, Y. Inoue and A. Kusenko, *Interstellar gas heating by primordial black holes*, *J. Cosmol. Astropart. Phys.* **2022** (2022) 017.
- [54] Y. Inoue and A. Kusenko, *New x-ray bound on density of primordial black holes*, *J. Cosmol. Astropart. Phys.* **2017** (2017) 034.
- [55] K. Inomata, M. Kawasaki and Y. Tada, *Revisiting constraints on small scale perturbations from big-bang nucleosynthesis*, *Phys. Rev. D* **94** (2016) 043527.
- [56] H. Niikura, M. Takada, N. Yasuda, R.H. Lupton, T. Sumi, S. More et al., *Microlensing constraints on primordial black holes with subaru/hsc andromeda observations*, *Nature Astronomy* **3** (2019) 524.
- [57] C. Alcock, R.A. Allsman, D.R. Alves, T.S. Axelrod, A.C. Becker, D.P. Bennett et al., *The MACHO project: Microlensing detection efficiency*, *The Astrophysical Journal Supplement Series* **136** (2001) 439.
- [58] M. Oguri, J.M. Diego, N. Kaiser, P.L. Kelly and T. Broadhurst, *Understanding caustic crossings in giant arcs: Characteristic scales, event rates, and constraints on compact dark matter*, *Phys. Rev. D* **97** (2018) 023518.
- [59] T. Nakama, B. Carr and J. Silk, *Limits on primordial black holes from  $\mu$  distortions in cosmic microwave background*, *Phys. Rev. D* **97** (2018) 043525.
- [60] S. Wang, Y.-F. Wang, Q.-G. Huang and T.G.F. Li, *Constraints on the primordial black hole abundance from the First Advanced LIGO Observation Run using the stochastic gravitational-wave background*, *Phys. Rev. Lett.* **120** (2018) 191102.
- [61] A. Hall, A.D. Gow and C.T. Byrnes, *Bayesian analysis of LIGO-Virgo mergers: Primordial versus astrophysical black hole populations*, *Phys. Rev. D* **102** (2020) 123524.
- [62] S. Young and C.T. Byrnes, *Initial clustering and the primordial black hole merger rate*, *J. Cosmol. Astropart. Phys.* **2020** (2020) 004.
- [63] G. Ballesteros, P.D. Serpico and M. Taoso, *On the merger rate of primordial black holes: effects of nearest neighbours distribution and clustering*, *J. Cosmol. Astropart. Phys.* **2018** (2018) 043.
- [64] G. Hütsi, M. Raidal and H. Veermäe, *Small-scale structure of primordial black hole dark matter and its implications for accretion*, *Phys. Rev. D* **100** (2019) 083016.
- [65] V. De Luca, G. Franciolini, P. Pani and A. Riotto, *Constraints on primordial black holes: The importance of accretion*, *Phys. Rev. D* **102** (2020) 043505.

- [66] P. Auclair and B. Blachier, *Small-scale clustering of primordial black holes: Cloud-in-cloud and exclusion effects*, *Phys. Rev. D* **109** (2024) 123538.
- [67] M. Raidal, V. Vaskonen and H. Veermäe, *Formation of primordial black hole binaries and their merger rates*, 2024.